Article

Integrating Polydopamine Nanosphere/Aptamers Nanoplatform with DNase-I-assisted Recycling Amplification Strategy for Simultaneous Detection of MMP-9 and MMP-2 During Renal Interstitial Fibrosis

Xie-an Yu, Yiting Hu, Ying Zhang, Ran Zhang, Xuefei Bai, Lifei Gu, Han Gao, Renshi Li, Jiangwei Tian, and Bo-Yang Yu

ACS Sens., **Just Accepted Manuscript** • DOI: 10.1021/acssensors.0c00058 • Publication Date (Web): 20 Mar 2020

Integrating Polydopamine Nanosphere/Aptamers Nanoplatform with DNase-I-assisted Recycling Amplification Strategy for Simultaneous Detection of MMP-9 and MMP-2 During Renal Interstitial Fibrosis

Xie-an Yu,†,‡ Yiting Hu,†,‡ Ying Zhang,† Ran Zhang,† Xuefei Bai,† Lifei Gu,† Han Gao,† Renshi Li,†,* Jiangwei Tian,†,* and Bo-Yang Yu†

† State Key Laboratory of Natural Medicines, Jiangsu Key Laboratory of TCM Evaluation and Translational Research, Research Center for Traceability and Standardization of TCMs, School of Traditional Chinese Pharmacy, China Pharmaceutical University, Nanjing 211198, P.R. China.

ABSTRACT: Matrix metalloproteinase-9 (MMP-9) and matrix metalloproteinase-2 (MMP-2) play important roles in the progression of renal interstitial fibrosis (RIF). There is an increasing demand to construct a novel method for simultaneous detection of MMP-9 and MMP-2 to monitor the progression of RIF. Herein, a strategy based on the nanoplatform composed of the polydopamine nanosphere and fluorescence labelled aptamers is developed to simultaneously detect MMP-9 and MMP-2 with DNase-I-assisted recycling signal amplification. In the light of tracing the recovered fluorescence intensity at 520 nm and 610 nm upon adding MMP-9 and MMP-2, the increased fluorescence intensity is linear to the different concentrations of MMP-9 and MMP-2 with the detection limits of 9.6 pg/mL and 25.6 pg/mL for MMP-9 and MMP-2, respectively. More intriguingly, the results of unilateral ureteral obstruction mice show that the concentration of MMP-9 in urine is increased with the extension of ligation time while the concentration of MMP-2 is reversed, indicating that the ratio of MMP-9/MMP-2 could be considered as the potential urinary biomarker to evaluate the progress of RIF and the therapeutic effect of Huangkui capsule on RIF. Therefore, this study provides a paradigmatic strategy for simultaneous detection of dual-markers of RIF, which is promising for auxiliary clinical diagnosis and assessment of prognosis of chronic kidney disease.

KEYWORDS: polydopamine nanosphere, MMP-9, MMP-2, biomarker, renal interstitial fibrosis

Renal fibrosis, particularly renal interstitial fibrosis (RIF) is the significant feature of progressive renal disease, which is regarded as the inevitable pathological pathway of chronic kidney disease (CKD).[1-6] The characteristics of RIF are the generation of massive myofibroblasts and the accumulation of excessive matrix proteins, gradually resulting in nephrons loss, renal function decline and even end-stage renal disease.[7-10] Hence, RIF is a major determinant and a reliable predictor of the prognosis of CKD. In the past several years, a wide number of studies have focused on the role of epithelial-mesenchymal transition (EMT) in RIF, begun to build a consensus that EMT prompted to appreciate the role in the evolution of RIF.[11-13] Throughout the EMT process, several extracellular factors and intracellular mediators controlling EMT were closely related to the disruption of tubular basement membrane (TBM) that accelerated the progressive of RIF and could also be explored in developing a new strategy for future antifibrotic therapeutics.[14-16] Therefore, if the integrity of TBM in the EMT can be effectively monitored, the RIF will be diagnosed and treated in time, thereby alleviating the advanced of CKD.

Matrix metalloproteases (MMPs) are the large family of proteases, which include gelatinases, stromelysins, collagenases, and membrane-type MMPs.[17,18] This family could synergistically degrade abundant extracellular matrix and is involved in various pathophysiological processes, which plays an essential role in tissue degradation and remodeling.[19,20] However, owing to the fact that MMP-9 and MMP-2 are the type IV collagen proteases that share the ability to degrade TBM mainly composed with IV collagen, during the process of RIF, MMP-9 and MMP-2 could disrupt the integrity of TBM,[21,22] which in turn promotes EMT of tubular epithelial

cell, and thus accelerating the progressive RIF. Accordingly, MMP-9 and MMP-2 have been treated as promoters of tubular epithelial cell EMT via TBM disruption.[23-25] Taking these characteristics of MMP-9 and MMP-2 into consideration, the contents of MMP-9 and MMP-2 in the process of EMT would reflect the integrity of TBM, offering the potential opportunity for the detection and intervention of RIF.

Currently, a large number of literatures for measuring MMP-9 or MMP-2 have been reported including western immunoblot,[26,27] immunostaining,[28,29] gelatin zymography,[30,31] ELISA kits[32,33] and fluorescent nanoprobe[34,35]. These detection methods are not only cumbersome and time consuming, but also requiring long-trained technicians[36,37]. Meanwhile, during the process of RIF, the change rule of MMP-9 or MMP-2 and the relationship between two proteases in the renal tissues and urine are insufficient. Therefore, it is urgent to develop a specific, sensitive and simple detection method for simultaneous detection of MMP-9 and MMP-2 in the hope of exploring the rule of two proteases in the renal tissues and urine during the progress of RIF.

Herein, we have constructed a novel nanoplatform based on the polydopamine nanosphere (PDANS) and fluorescence labelled aptamers to simultaneously detect MMP-9 and MMP-2 with DNase-I-assisted recycling amplification (Scheme 1). The two

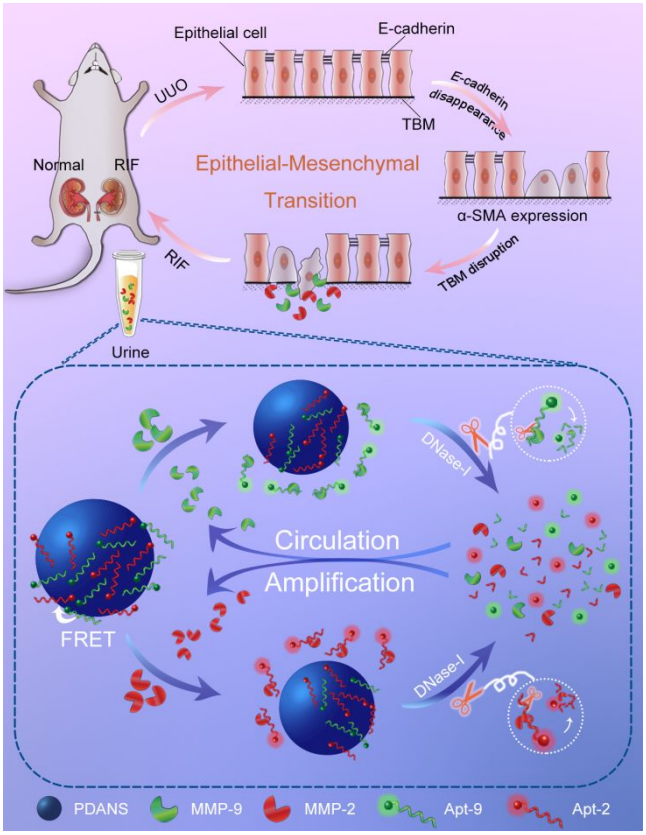

Scheme 1. Schematic of Apt-9/Apt-2/PDANS nanoplatform for simultaneous detection of MMP-9 and MMP-2 during RIF with DNase-I-assisted recycling amplification

aptamers (against MMP-9 and MMP-2) are single stranded DNA (ssDNA) sequences and labelled with 5-carboxyfluorescein (FAM) and Texas Red, respectively. The fluorophore-labelled aptamers are adsorbed on the surface of PDANS through π-π deposition and hydrogen bonding, and PDANS can efficiently quench fluorophores based on Förster resonance energy transfer (FRET) principle. Then, in the presence of targets (MMP-9 and MMP-2), the aptamer can specifically bind to their corresponding targets to form the aptamer/target complexes, leading to the release of aptamers from the surface of PDANS and the fluorescence recovery. At the same time, in order to improve the detection sensitivity, the DNase-I was introduced to the system to selectively hydrolyze the aptamers dissociated from PDANS. Subsequently, the released targets might further interact with residual aptamer on the surface of PDANS, triggering the abundant fluorescence and realizing the signal amplification. Finally, this method has been successfully applied to detect MMP-9 and MMP-2 in urine and tissue homogenate of unilateral ureteral obstruction (UUO) mice. It was found that the contents of MMP-9 and MMP-2 were increased with the extension of ligation times in tissue homogenate of UUO mice. The results of UUO mice showed that the concentration of MMP-9 in urine was increased with the extension of ligation times while the concentration of MMP-2 was reversed, indicating that the ratio of MMP-9/MMP-2 could be considered

as the new potential urinary biomarker for evaluating the progress of RIF. Thus, MMP-9/MMP-2 would be helpful for auxiliary clinical diagnosis and assessment of prognosis of CKD, and this strategy also holds great potentialities for clinical diagnosis of RIF and evaluating therapeutic effect of Huangkui capsule for CKD.

EXPERIMENTAL SECTION

Materials and reagents. Dopamine hydrochloride, Deoxyribonuclease-I (DNase-I), 1 M Tris-HCl (pH 7.4) were obtained from Solarbio (Beijing, China). FAM-labelled MMP-9 aptamer,[38] Apt-9 (5'-FAM-TAC GGC CGC ACG AAA AGG TGC CCC ATA ACT CAA TGC CGT A-3') and Texas Red-labelled MMP-2 aptamer,[39] Apt-2 (5'-Texas Red-TCG CCG TGT AGG ATT AGG CCA GGT ATG GGA ACC CGG TAA C-3') were synthesized by Shanghai Sangon Biotechnology Co. (Shanghai, China). The TGF-β protein was acquired by Sino Biological Inc. (Beijing, China). MMP-9 ELISA kit and MMP-2 ELISA kit were purchased from Zhuo Cai Biotechnology Co., Ltd. (Shanghai, China). The 96 microwell plates were offered from Coring Incorporated (New York, U.S.A.). Ultrapure water (electric resistance = 18.25 MΩ) obtaining via a Millipore Milli-Q water purification system (Billerica, MA, U.S.A.) was used throughout the experiments.

Instruments. The absorption spectra were recorded on a Cary Series UV-vis spectrophotometer (Agilent Technologies, USA). The Excitation and emission spectra were measured on Cary Eclipse Fluorescence Spectrophotometer (Agilent Technologies Inc., USA). The morphology of PDANS was featured at a JEOL JEM-200CX transmission electron microscope (TEM) worked at 200 kV. Then the solution of PDANS was dropped onto a carbon-coated copper grid for TEM measurement. The size of PDANS was determined by dynamic light scattering (DLS) using a Mastersizer 2000 particle size analyzer. The zeta potential was tested on a Malvern Zeta sizer-Nano Z instrument (Nano-Z, Malvern, UK). Fourier transform infrared (FT-IR) spectra were performed on a Bruker Tensor 27 FTIR spectrometer. Confocal fluorescence imaging of HK-2 cells was carried on a confocal laser scanning microscope (CLSM, LSM800, Zeiss, Germany). The fluorescence intensity was read on Varioskan Flash (Thermo, USA). The Masson staining images were obtained on a digital pathology slice scanner using NanoZoomer 2.0 RS (Hamamatsu, China).

Synthesis of PDANS. According to previous reports,[40-42] PDANS were synthesized via self-aggregation. Briefly, 100 mg of dopamine hydrochloride was added to the mixture of 100 mL of Tris-HCl buffer (10 mM pH 8.0) and 40 mL of isopropyl alcohol with continuous stirring. After stirring for 48 h, the polydopamine nanosphere was preliminarily obtained. Then, the solution was centrifuged and washed/resuspended with water for several times. Finally, the precipitate was dried for further experiments.

Preparation of the Apt-9/Apt-2/PDANS nanocomplex. After the synthesis of PDANS, PDANS was introduced into 100 nM Apt-9 and 100 nM Apt-2 and incubated at room temperature for 30 seconds to quench the fluorescence and form the Apt-9/Apt-2/PDANS nanocomplex.

Simultaneous detection of MMP-9 and MMP-2. Different concentrations of MMP-9 (ranging from 24 to 6000 pg/mL) and MMP-2 (ranging from 64 to 16000 pg/mL) were added into Apt-9/Apt-2/PDANS nanocomplex in the binding buffer. Then, 10 units of DNase-I was added to the solution and incubated at 37 ℃ for 120 mins. Finally, the fluorescence intensities were detected. For the recovery measurement, negative urine and tissue samples were spiked with MMP-9 and MMP-2 for analysis. The recovery% was calculated via equation: Recovery (%) = (Measured-Original)/ Spiked ×100%. (Measured: the concentration of MMP-9 or MMP-2 when supplemented with standard protein. Original: the concentration of MMP-9 or MMP-2 when no spiked with standard protein.)

Detection of MMP-9 and MMP-2 in urine of UUO mice. Thirty-six male mice were randomly divided into six groups: (1) the sham-operated group (n=6, only freed the ureter without ligated); (2) the 3-day ligation group (n=6); (3) the 5-day ligation group (n=6); (4) the 7-day ligation group (n=6); (5) the 14-day ligation group (n=6); (6) the administration group (n=6, ligated the left ureter and orally administrated Huangkui capsules for 14 days, dosage: 1.5 g/kg).

According to the literature,[2] the mice were anesthetized by intraperitoneal injection of 1% sodium pentobarbital and put on the operating table. After partial shaving, the mice were routinely sterilized with iodophor. The left abdomen was opened to expose the left kidney. Then, the ureter was exposed and double ligated with suture. Finally, the incision was sutured layer by layer with disinfection of iodophor.

The urine of mice from different groups was collected daily by bladder extrusion method. Then, the collected urine samples were centrifuged at 3000 rpm for 10 mins. 10 μL urinary supernatant of each mouse was added to the Apt-9/Apt-2/PDANS nanoplatform with 10 U DNase-I in the buffer and incubated at 37 ℃ for 120 mins. The fluorescence value was measured by microplate reader. The concentrations of MMP-9 and MMP-2 were calculated

by standard curve respectively. Moreover, the contents of MMP-9 and MMP-2 in urine were detected according to the protocols provided by MMP-9 ELISA kit and MMP-2 ELISA kit.

Detection of MMP-9 and MMP-2 in kidney tissue homogenate and Masson staining analysis. The mice of each group were sacrificed at 3, 5, 7 and 14 day after surgery. The left kidneys of mice in each group were stripped and weighed. The half part kidneys of each group were placed in 10% formalin solution for the Masson pathological staining. The rest part kidney tissue was cut and placed in a −80 ℃ freezer for storage.

The kidney tissue was taken out from the −80 ℃ refrigerator and extracted in a homogenizer. The homogenate supernatant was collected after centrifuged at 3000 rpm for 10 mins. Afterwards, the supernatant was diluted 5 times and then incubated with Apt-9/Apt-2/PDANS nanoplatform with 10 U DNase-I in the buffer at 37 ℃ for 120 mins. The concentrations of MMP-9 and MMP-2 were calculated by standard curve respectively according to the fluorescence value by the microplate reader. Furthermore, the contents of MMP-9 and MMP-2 in tissue homogenate were detected according to the protocols provided by MMP-9 ELISA kit and MMP-2 ELISA kit.

Confocal fluorescence imaging for HK-2 cells. The HK-2 cells were seeded into 35 mm confocal dishes with a density of 4×10^4 per dish and incubated at 37 ℃. One group of cells was incubated with PDANS, and another group was co-incubated with Apt-9/Apt-2/PDANS for 12 h at 37 ℃. Meanwhile, the cells were stimulated with TGF-β (20 ng/mL) for 24 h and then incubated with Apt-9/Apt-2/PDANS at 37 ℃ for 12 h. After incubation, the cells were stained with 50 μg/mL Hoechst 33342 for 30 mins to perform fluorescence imaging with a CLSM. Hoechst 33342 was excited at 405 nm and the emission was measured from 420 to 460 nm. FAM was excited at 488 nm and the emission was collected from 500 to 540 nm. Texas Red was excited at 550 nm and the emission was collected from 610 to 650 nm. All images were analyzed by the ZEN imaging software.

RESUITS AND DISCUSSION

Synthesis and characterization of nanoplatform. The PDANS was synthesized by self-aggregation of dopamine in the mixed solution contained with Tris-HCl buffer and isopropyl alcohol. The solution of PDANS was dropped onto a carbon-coated copper grid for TEM measurement. TEM images of PDANS showed well-dispersed spherical morphology with the diameter of 260 ± 12.5 nm (Figure 1A and 1B) and the aptamers (Apt-9 and Apt-2) were absorbed on the surface of PDANS (Figure S1). The dynamic light scattering (DLS) revealed that the average hydrodynamic diameters of PDANS and Apt-9/Apt-2/PDANS were 260 nm (Figure 1B) and 268 nm (Figure S2), respectively. Furthermore, the zeta potential of PDANS and Apt-9/Apt-2/PDANS were −35.6 mV (Figure S3) and −42.3 mV (Figure S4), respectively. The infrared characteristic peaks of dopamine between 500 and 1700 cm^{-1} were nearly disappeared after polymerization, illustrating the successful synthesis of PDANS (Figure 1D). Additionally, PDANS showed non-aggregating (Figure S5) and sustained the ability of fluorescence quenching (Figure S6) after stored for 2 weeks, suggesting the high stability of PDANS.

Owing to the π-π stacking and hydrogen bonding interactions between aptamers and PDANS, the Apt-9 and Apt-2 can absorb on the surface of PDANS. PDANS showed a broad UV-VIS-NIR absorption spectrum (Figure S7) which was overlapped well with the emission fluorescence spectrum of Apt-9 and Apt-2 (Figure S8), indicating that PDANS was a good quencher for Apt-9 and Apt-2. The excitation and emission fluorescence spectrum of Apt-9 (Figure S9) and Apt-2 (Figure S10) were also recorded. Furthermore, the progress of fluorescence quenching for Apt-9 and Apt-2 was very fast (Figure S11), which only took 30 seconds to achieve the equilibrium. Following that, the fluorescence quenching ability of PDANS toward Apt-9 (Figure 2A) and Apt-2 (Figure 2B) was also validated. The fluorescence intensities of 100 nM Apt-9 and 100 nM Apt-2 were decreased with an increasing concentration of PDANS. The quenching efficiency was almost 98% in the presence of 0.3 mg/mL of PDANS (Figure S12 and S13), indicating the effective quenching ability of PDANS to labelled-aptamers. Consequently, 0.3 mg/mL PDANS, 100 nM Apt-9 and 100 nM Apt-2 were considered as the optimal conditions for the subsequent experiments.

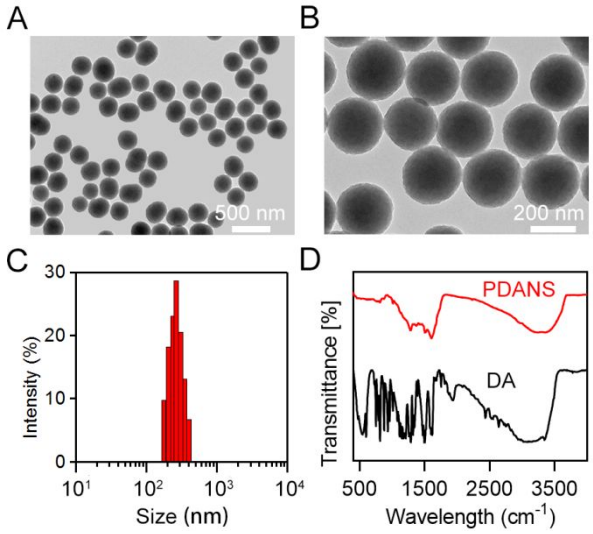

Figure 1. (A) and (B) TEM images of the PDANS. (C) The hydrodynamic size of PDANS determined by DLS. (D) IR spectra of PDANS and DA.

Performance of Apt-9/Apt-2/PDANS nanoplatform for MMP-9 and MMP-2 detection. After forming the Apt-9/Apt-2/PDANS, the nanoplatform was applied to detect MMP-9 and MMP-2. In the presence of targets, Apt-9 and Apt-2 could specifically react with targets and release from the surface of PDANS. Hence, simultaneous determination of multiple targets can be realized via tracing the fluorescence recovery of Apt-9 and Apt-2. In contrast, after adding targets and 10 U DNase-I, Apt-9 and Apt-2 desorbed from the surface of PDANS were selectively digested by DNase-I. Subsequently, the targets were dissociative again, which could continue to combine the rest of aptamer on the surface of PDANS and repeat the cyclic reaction, resulting in recycling amplification of signal (Figure 2C and 2D). Notably, the addition of single DNase-I did not result in the fluorescence signal recovery, which demonstrated that aptamer adsorbed on the surface of PDANS could be effectively protected from enzymatic cleavage. The histograms of fluorescence intensities recovered at 520 nm (Figure S14) and 610 nm (Figure S15) were separately monitored, further revealing the simultaneous determination of multiple proteases with DNase-I-assisted recycling amplification strategy.

With an increasing time of adding targets and DNase-I, the fluorescence intensity gradually recovered and finally reached the equilibrium at 120 min (Figure S16 and S17). Hence, the optimal reaction time was 120 min. With the increase in the concentrations of MMP-9 from 0 to 6 ng/mL and MMP-2 from 0 to 16 ng/mL, the emission peaks at 520 nm of FAM (Figure 3A) and 610 nm of Texas Red (Figure 3B) increased gradually. Apt-9 fluorescence intensity was found to be linear with the concentration of MMP-9 in the range of 24-600 pg/mL with the limit detection of 9.6 pg/mL (Figure 3C) and Apt-2 fluorescence intensity was linear with the concentration of MMP-2 in the range of 64-1600 pg/mL with the limit detection of 25.6 pg/mL (Figure 3D), respectively.

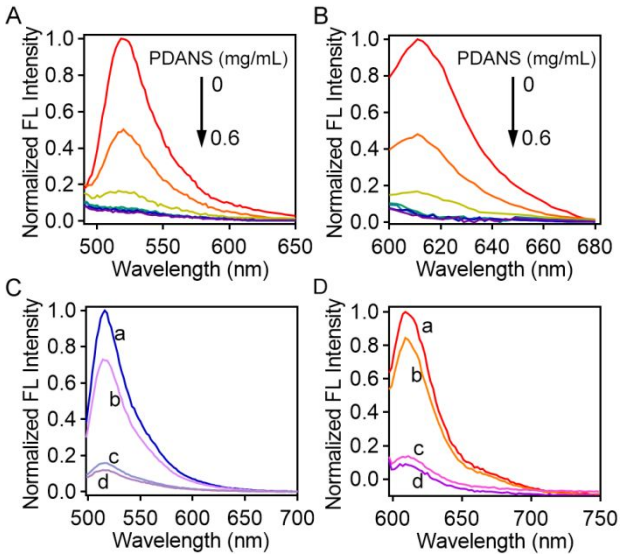

Figure 2. Fluorescence emission spectra of Apt-9 (A) and Apt-2 (B) with increasing concentrations of PDANS (0, 0.05, 0.15, 0.3, 0.4, 0.5, 0.6 mg/mL). (C) Fluorescence emission spectra of Apt-9 after the Apt-9/Apt-2/PDANS were incubated in different conditions (a: Apt-9/Apt-2/PDANS + DNase-I + MMP-9; b: Apt-9/Apt-2/PDANS + MMP-9; c: Apt-9/Apt-2/PDANS + DNase-I; d: Apt-9/Apt-2/PDANS). (D) Fluorescence emission spectra of Apt-2 after the Apt-9/Apt-2/PDANS were incubated in different conditions (a: Apt-9/Apt-2/PDANS + DNase-I + MMP-2; b: Apt-9/Apt-2/PDANS + MMP-2; c: Apt-9/Apt-2/PDANS + DNase-I; d: Apt-9/Apt-2/PDANS).

Furthermore, the specificity of nanoplatform for simultaneous detection of MMP-9 and MMP-2 was investigated. MMP-9 was capable of the recovery of fluorescence intensity to Apt-9, while after incubation with Scr, FBS, NGAL, DNase-I, MMP-2 for 120 mins, the fluorescence intensity of Apt-9 almost remained unchanged (Figure S18). Similarly, Apt-2 was only responded to MMP-2 which induced the fluorescence enhancement (Figure S19).

Additionally, the recovery assay was also performed to assess the reliability of this method in the detection of MMP-9 and MMP-2 in urine and tissue. The experimental results showed that the recovery with the rate was more that 90% in urine (Table S1) and tissue (Table S2). Accordingly, these results demonstrated that PDANS/aptamers nanoplatform was able to selective detection of MMP-9 and MMP-2 in the complex system, which offered the tangible evidence for simultaneous detection of MMP-9 and MMP-2 in complex biological samples.

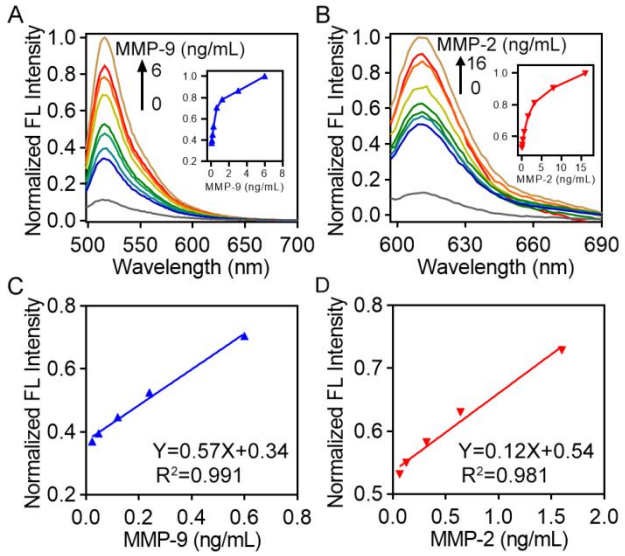

Figure 3. Fluorescence spectra of Apt-9 (A) and Apt-2 (B) after the Apt-9/Apt-2/PDANS in the presence of DNase-I was incubated with different concentrations of MMP-9 and MMP-2, respectively. Linear curves for MMP-9 (C) and MMP-2 (D) detection, respectively.

Detection of MMP-9 and MMP-2 in urine of UUO mice. UUO model is an ideal model for studying the mechanism of RIF. Besides, Huangkui (HK) capsule, extracted from the flower of *A. manihot*, could protect RIF of CKD owing to the involvement in the mechanism of inhibiting ROS and ERK pathway.[43] Hence, Huangkui capsule was selected to explore the impact on the concentrations of MMP-9 and MMP-2 during RIF. By recording the body weight of each group of mice, the result showed that the sham-operated mice grew well, while the obstruction mice grew slowly (Figure S20). Meanwhile, we harvested the left obstruction kidney and calculated the ratio of kidney weight/body weight (KW/BW) of mice in each group. The KW/BW of the obstruction group was lower than sham-operated group, while the KW/BW of the HK administration group was enhanced comparing with obstruction group (Figure S21). The above results indicated that the UUO model was established successfully.

The collecting urine samples were added to the constructed nanoplatform and incubated for 120 mins at 37 ℃. The histograms indicated that the levels of MMP-9 and MMP-2 were the lowest in sham-operated group. However, with the obstruction times going on, the content of MMP-9 raised gradually (Figure 4A), while the concentration of MMP-2 was in an opposite tendency (Figure 4B). Meanwhile, the level of MMP-9 was decreased and the content of MMP-2 was increased in the administration group (Huangkui capsule) compared with the ligation 14-day group. Based on above results, we analyzed and calculated the ratio of the content of MMP-9/MMP-2 (Figure S22). The result displayed that MMP-9/MMP-2 was gradually increased which showed an obvious trend with the extension of ligation time comparing to the single marker, indicating that MMP-9/MMP-2 could be selected as the potential biomarker in urine. In addition, the MMP-9 and MMP-2 ELISA kits were applied to confirm the concentrations of MMP-9 and MMP-2 in urine. The results demonstrated that the change rules of the concentrations of MMP-9 and MMP-2 in urine were almost consistent with results based on the nanoplatform (Figure S23 and S24).

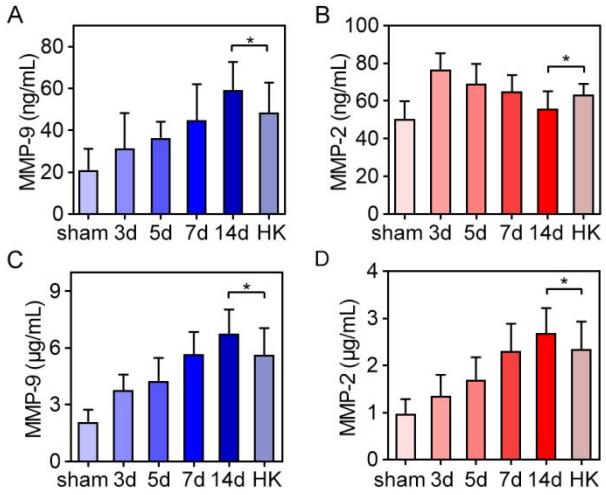

Figure 4. Concentrations of MMP-9 (A) and MMP-2 (B) after the Apt-9/Apt-2/PDANS in the presence of DNase-I was incubated with urine of different groups. Concentrations of MMP-9 (C) and MMP-2 (D) after the Apt-9/Apt-2/PDANS in the presence of DNase-I was incubated with kidney homogenate of different groups. Data are means ± SD (n=6, $*P < 0.05$ for 14-day ligation group compared to the administration group using a Student's *t* test).

Detection of MMP-9 and MMP-2 in kidney tissue homogenate. The levels of MMP-9 and MMP-2 in kidney homogenate were also examined. The homogenate samples of mice in each group were diluted 5 times and were added to the constructed nanoplatform incubating for 120 mins at 37 ℃. As shown in Figure 4C and 4D, the contents of MMP-9 and MMP-2 remained lowest in sham-operated group. However, the concentrations of MMP-9 and MMP-2 were in a gradually increased trend with the prolongation of ligation time. Meanwhile, the contents of MMP-9 and MMP-2 were decreased in administration group contrasted with 14-day ligation group, indicating that Huangkui capsule could effectively alleviate the progress of RIF through reducing the contents of MMP-9 and MMP-2. Similarly, MMP-9 ELISA kit and MMP-2 ELISA kit were used to detect the tissue homogenate (Figure S25 and S26). These results were consistent with our experimental data, verifying the reliability of our nanoplatform.

Moreover, Masson staining was performed to observe the progression of fibrosis in renal tissues (Figure 5A). In sham-operated group, only a small amount of blue staining was observed. In 3-day ligation group, the renal interstitial blue area staining was increased. With the obstruction prolonged, the blue staining area further enhanced at 7-day and 14-day ligation groups. However, the blue staining area was reduced in administration group compared with 14-day ligation group. At the same time, the Image Pro Plus pathological image analysis software was adopted to calculate the detail relative area of interstitial fibrosis positive staining in different groups. The result illustrated that the relative fibrosis area of interstitial fibrosis was increased gradually with the progress of RIF, while the relative fibrosis area of administration group was reduced in contrast to 14-day ligation group (Figure 5B and 5C).

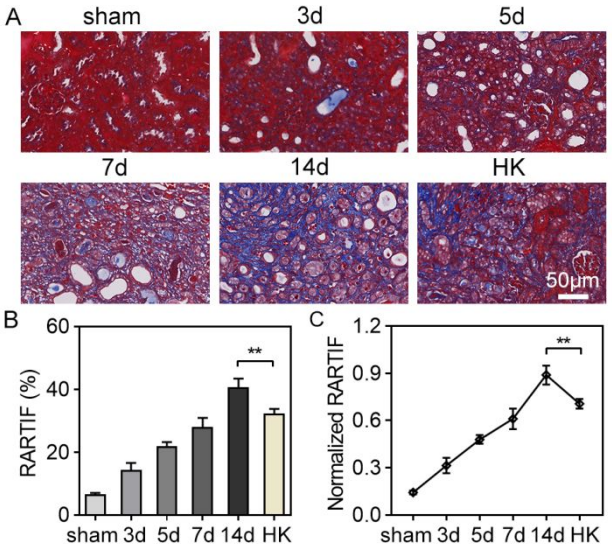

Figure 5. (A) Masson staining of the renal tissue sections from different group. Scale bars: 50 μm. (B) Relative area of renal tubular interstitial fibrosis (RARTIF) from different groups. (C) Normalized relative area of renal tubular interstitial fibrosis (RARTIF) from different groups. Data are means ± SD (n=9, $^{**}P < 0.01$ for 14-day ligation group compared to the administration group using a Student's *t* test).

Fluorescence imaging in HK-2 cells. The nanoplatform was also applied to image cells by fluorescence confocal microscopy (Figure 6). The cytotoxicities of PDANS and Apt-9/Apt-2/PDANS to HK-2 cells were evaluated using methylthiazolyl tetrazolium (MTT) assay. After incubation for 12 h, the cell viability of HK-2 cells could maintained at more than 95% with PDANS concentrations up to 0.3 mg/mL (Figure S27), indicating the good biocompatibility of PDANS and Apt-9/Apt-2/PDANS to HK-2 cells. Then the result showed that there was almost no fluorescence signal in HK-2 cells co-incubated with PDANS or Apt-9/Apt-2/PDANS. After HK-2 cells stimulated with TGF-β, the obvious FAM fluorescence signal was acquired from the HK-2 cells co-incubated with Apt-9/Apt-2/PDANS, but only with a weak Texas Red fluorescence signal. Zheng group[27] based on human kidney glomerular endothelial cells and Yang group[44] based on HK-2 cells both indicated that TGF-β mainly promoted MMP-9 production. It was revealed that the Apt-9/Apt-2/PDANS nanoplatform could sense the MMP-9 and MMP-2 successfully in the HK-2 cells.

CONCLUSION

In summary, the nanoplatform has been constructed based on PDANS and aptamers with DNase-I-assisted recycling amplification for simultaneously detecting multi-markers during the RIF. Compared with the conventional assay method, Apt-9/Apt-2/PDANS is a sensitive and selective nanoplatform for simultaneously detecting MMP-9 and MMP-2 in the urine, tissue homogenate and cells. Additionally, the nanoplatform is equipped with some virtues including simple preparation, easy operation, time saving and low cost. Hence, the current strategy can play an important role in RIF clinic diagnostics and evaluation of therapeutic effect of drug on RIF, contributing to relieve the progression of CKD in the future.

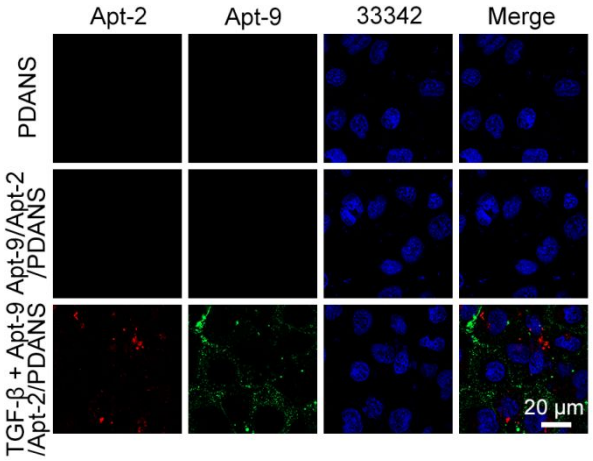

Figure 6. Confocal fluorescence images of HK-2 cells. Scale bars: 20 μm.

ASSOCIATED CONTENT

Supporting Information

The Supporting Information is available free of charge at http://pubs.acs.org.

Zeta potential of PDANS; the stability of PDANS; absorbance spectra of DA and PDANS; excitation and emission fluorescence spectra of Apt-9 and Apt-2; quenching efficiency of 100 nM Apt-9 and Apt-2; optimization of the experimental parameters;

selectivity analysis of the nanoplatform in the presence of different protein; concentrations of MMP-9 and MMP-2 in urine with ELISA kits; concentrations of MMP-9 and MMP-2 in kidney homogenate with ELISA kits;

AUTHOR INFORMATION

Corresponding Author

* E-mail: li-renshi@cpu.edu.cn (R. Li).
* E-mail: jwtian@cpu.edu.cn (J. Tian).

Author Contributions

‡ X.Y. and Y.H. contributed equally to this work.

Notes

Any additional relevant notes should be placed here.

ACKNOWLEDGMENT

This research was supported by National Natural Science Foundation of China (21775166), Natural Science Foundation for Distinguished Young Scholars of Jiangsu Province (BK20180026), and "Double First-Class" University Project (CPU2018GF06, CPU2018GY32).

REFERENCES

(1) Wu, Y. L.; Xie, J.; An, S. W.; Oliver, N.; Barrezueta, N. X.; Lin, M. H.; Birnbaumer, L.; Huang, C. L. Inhibition of TRPC6 channels ameliorates renal fibrosis and contributes to renal protection by soluble klotho. *Kidney Int.*, **2017**, *91*, 830-841.

(2) Chevalier, R. L.; Forbes, M. S.; Thornhill, B. A. Ureteral obstruction as a model of renal interstitial fibrosis and obstructive nephropathy. *Kidney Int.*, **2009**, *75*, 1145-1152.

(3) Humphreys, B. D. Mechanisms of renal fibrosis. *Annu. Rev. Physiol.*, **2018**, *80*, 309-326.

(4) Martínez-Klimova, E.; Aparicio-Trejo, O. E.; Tapia, E.; Pedraza-Chaverri, J. Unilateral ureteral obstruction as a model to investigate fibrosis-attenuating treatments. *Biomolecules*, **2019**, *9*, 141.

(5) Liu, Y. H. Cellular and molecular mechanisms of renal fibrosis. *Nat. Rev. Nephrol.*, **2011**, *7*, 684-696.

(6) Liu, Y. H. Renal fibrosis: New insights into the pathogenesis and therapeutics. *Kidney Int.*, **2006**, *69*, 213-217.

(7) Djudjaj, S.; Boor, P. Cellular and molecular mechanisms of kidney fibrosis. *Mol. Aspects Med.*, **2019**, *65*, 16-36.

(8) Lelongt, B.; Legallicier, B.; Piedagnel, R.; Ronco, P. M. Do matrix metalloproteases MMP-2 and MMP-9 (gelatinases) play a role in renal development, physiology and glomerular diseases? *Curr. Opin. Nephrol. Hypertens.*, **2001**, *10*, 7-12.

(9) Gu, L.; Wang, Y.; Yang, G.; Tilyek, A.; Zhang, C.; Li, S.; Yu, B.; Chai, C.; Cao, Z. Ribes diacanthum Pall (RDP) ameliorates UUO-induced renal fibrosis via both canonical and non-canonical TGF-β signaling pathways in mice. *J. Ethnopharmacol.*, **2019**, *231*, 302-310.

(10) Gewin, L. S. Renal fibrosis: Primacy of the proximal tubule. *Matrix Biol.*, **2018**, *68-69*, 248-262.

(11) Yang, J.; Liu, Y. Dissection of key events in tubular epithelial to myofibroblast transition and its implications in renal interstitial fibrosis. *Am. J. Pathol.*, **2001**, *159*, 1465-1475.

(12) Qi, R.; Yang, C. Renal tubular epithelial cells: the neglected mediator of tubulointerstitial fibrosis after injury. *Cell Death Dis.*, **2018**, *9*, 1126.

(13) Zhou, D.; Liu, Y. Understanding the mechanisms of kidney fibrosis. *Nat. Rev. Nephrol.*, **2016**, *12*, 68-70.

(14) Liu, Y. New insights into epithelial-mesenchymal transition in kidney fibrosis. *J. Am. Soc. Nephrol.*, **2010**, *21*, 212-222.

(15) Liu, Y. Epithelial to mesenchymal transition in renal fibrogenesis: pathologic significance, molecular mechanism, and therapeutic intervention. *J. Am. Soc. Nephrol.*, **2004**, *15*, 1-12.

(16) Zeisberg, M.; Bonner, G.; Maeshima, Y.; Colorado, P.; Müller, G. A.; Strutz, F.; Kalluri, R. Collagen composition and assembly regulates epithelial-mesenchymal transdifferentiation. *Am. J. Pathol.*, **2001**, *159*, 1313-1321.

(17) Ronco, P.; Chatziantoniou, C. Matrix metalloproteases and matrix receptors in progression and reversal of kidney disease: therapeutic perspectives. *Kidney Int.*, **2008**, *74*, 873-878.

(18) Giannandrea, M.; Parks, W. C. Diverse functions of matrix metalloproteases during fibrosis. *Dis. Model Mech.*, **2014**, *7*, 193-203.

(19) Tan, R. J.; Liu, Y. Matrix metalloproteases in kidney homeostasis and diseases. *Am. J. Physiol. Renal Physiol.*, **2012**, *302*, 1351-1361.

(20) Afratis, N. A.; Selman, M.; Pardo, A.; Sagi, I. Emerging insights into the role of matrix metalloproteases as therapeutic targets in fibrosis. *Matrix Biol.*, **2018**, *68-69*, 167-179.

(21) Zeisberg, M.; Maeshima, Y.; Mosterman, B.; Kalluri, R. Extracellular matrix microenvironment regulates migratory behavior of activated tubular epithelial cells. *Am. J. Pathol.*, **2002**, *160*, 2001-2008.

(22) Zeisberg, M.; Neilson, E. G. Mechanisms of tubulointerstitial fibrosis. *J. Am. Soc. Nephrol.*, **2010**, *21*, 1819-1834.

(23) Cheng, Z.; Limbu, M. H.; Wang, Z.; Liu, J.; Liu, L.; Zhang, X.; Chen, P.; Liu, B. MMP-2 and 9 in chronic kidney disease. *Int. J. Mol. Sci.*, **2017**, *18*, 776.

(24) Cheng, S.; Pollock, A. S.; Mahimkar, R.; Olson, J. L.; Lovett, D. H. Matrix metalloproteinase 2 and basement membrane integrity: a unifying mechanism for progressive renal injury. *FASEB J.*, **2006**, *20*, 1898-1900.

(25) Tan, T. K.; Zheng, G.; Hsu, T. T.; Wang, Y.; Lee, V. W.; Tian, X.; Wang, Y.; Cao, Q.; Wang, Y.; Harris, D. C. Macrophage matrix metalloproteinase-9 mediates epithelial-mesenchymal transition in vitro in murine renal tubular cells. *Am. J. Pathol.*, **2010**, *176*, 1256-1270.

(26) Du, X.; Shimizu, A.; Masuda, Y.; Kuwahara, N.; Arai, T.; Kataoka, M.; Uchiyama, M.; Kaneko, T.; Akimoto, T.; Lino, Y.; Fukuda, Y. Involvement of matrix metalloproteinase-2 in the development of renal interstitial fibrosis in mouse obstructive nephropathy. *Lab. Invest.*, **2012**, *92*, 1149-1160.

(27) Zhao, Y.; Qiao, X.; Wang, L.; Tan, T. K.; Zhao, H.; Zhang, Y.; Zhang, J.; Rao, P.; Cao, Q.; Wang, Y.; Wang, Y.; Wang, Y. M.; Lee, V. W.; Alexander, S. I.; Harris, D. C.; Zheng, G. Matrix metalloproteinase 9 induces endothelial-mesenchymal transition via Notch activation in human

kidney glomerular endothelial cells. *BMC Cell Biol.*, **2016**, *17*, 21.
(28) Wang, X.; Zhou, Y.; Tan, R.; Xiong, M.; He, W.; Fang, L.; Wen, P.; Jiang, L.; Yang, J. Mice lacking the matrix metalloproteinase-9 gene reduce renal interstitial fibrosis in obstructive nephropathy. *Am. J. Physiol. Renal Physiol.*, **2010**, *299*, 973-982.
(29) Cheng, S.; Lovett, D. H. Gelatinase A (MMP-2) is necessary and sufficient for renal tubular cell epithelial-mesenchymal transformation. *Am. J. Pathol.*, **2003**, *162*, 1937-1949.
(30) Tan, T. K.; Zheng, G. P.; Hsu, T. T.; Lee, S. R.; Zhang, J.; Zhao, Y.; Tian, X.; Wang, Y.; Wang, Y. M.; Cao, Q.; Wang, Y.; Lee, V. W.; Wang, C.; Zheng, D.; Alexander, S. I.; Thompson, E.; Harris, D. C. Matrix metalloproteinase-9 of tubular and macrophage origin contributes to the pathogenesis of renal fibrosis via macrophage recruitment through osteopontin cleavage. *Lab. Invest.*, **2013**, *93*, 434-449.
(31) Zhao, Y.; Qiao, X.; Tan, T. K.; Zhao, H.; Zhang, Y.; Liu, L.; Zhang, J.; Wang, L.; Cao, Q.; Wang, Y. P.; Wang, Y.; Wang, Y. M.; Lee, V. W. S.; Alexander, S. I.; Harris, D. C. H.; Zheng, G. P. Matrix metalloproteinase 9-dependent Notch signaling contributes to kidney fibrosis through peritubular endothelial-mesenchymal transition. *Nephrol. Dial. Transplant.*, **2017**, *32*, 781-791.
(32) Chang, H. R.; Yang, S. F.; Li, M. L.; Lin, C. C.; Hsieh, Y. S.; Lian, J. D. Relationships between circulating matrix metalloproteinase-2 and -9 and renal function in patients with chronic kidney disease. *Clin. Chim. Acta.*, **2006**, *366*, 243-248.
(33) Bienias, B.; Sikora, P. Urinary metalloproteases and tissue inhibitors of metalloproteases as potential early biomarkers for renal fibrosis in children with nephrotic syndrome. *Medicine*, **2018**, *97*, 8.
(34) Pan, W.; Yang, H.; Li, N.; Yang, L.; Tang, B. Simultaneous visualization of multiple mRNAs and matrix metalloproteinases in living cells Using a fluorescence nanoprobe. *Chemistry.*, **2015**, *21*, 6070-6073.
(35) Luan, M.; Li, N.; Pan, W.; Yang, L.; Yu, Z.; Tang, B. Simultaneous detection of multiple targets involved in the PI3K/AKT pathway for investigating cellular migration and invasion with a multicolor fluorescent nanoprobe. *Chem Commun.*, **2016**, *53*, 356-359.
(36) Yu, Z.; Cai, G.; Tong, P.; Tang, D. Saw-toothed microstructure-based flexible pressure sensor as the signal readout for point-of-Care immunoassay. *ACS Sens.*, **2019**, *4*, 2272-2276.
(37) Cai, G.; Yu, Z.; Ren, R.; Tang, D. Exciton-plasmon interaction between AuNPs/Graphene nanohybrids and CdS Quantum Dots/TiO2 for photoelectrochemical aptasensing of Prostate-Specific Antigen. *ACS Sens.*, **2018**, *3*, 632-639.
(38) Duellman, T.; Chen, X.; Wakamiya, R.; Yang, J. Nucleic acid-induced potentiation of matrix metalloproteinase-9 enzymatic activity. *Biochem. J.*, **2018**, *475*, 1597-1610.
(39) Han, M. E.; Baek, S.; Kim, H. J.; Lee, J. H.; Ryu, S. H.; Oh, S. O. Development of an aptamer-conjugated fluorescent nanoprobe for MMP2. *Nanoscale Res. Lett.*, **2014**, *9*, 104.
(40) Qiang, W. B.; Li, W.; Li, X. Q.; Chen, X.; Xu, D. K. Bioinspired polydopamine nanospheres: a superquencher for fluorescence sensing of biomolecules. *Chem. Sci.*, **2014**, *5*, 3018.
(41) Yan, J.; Yang, L.; Lin, M. F.; Ma, J.; Lu, X.; Lee, P. S. Polydopamine spheres as active templates for convenient synthesis of various nanostructures. *Small*, **2013**, *9*, 596-603.
(42) Yang, L.; Ren, Y.; Pan, W.; Yu, Z.; Tong, L.; Li, N.; Tang, B. Fluorescent nanocomposite for visualizing cross-talk between microRNA-21 and hydrogen peroxide in ischemia-reperfusion injury in live cells and in vivo. *Anal Chem.*, **2016**, *88*, 11886-11891.
(43) Cai, H. D.; Su, S. L.; Qian, D. W.; Guo, S.; Tao, W. W.; Cong, X. D.; Tang, R.; Duan, J. A. Renal protective effect and action mechanism of Huangkui capsule and its main five flavonoids. *J. Ethnopharmacol.*, **2017**, *206*, 152-159.
(44) Tian, Y. C.; Chen, Y. C.; Chang, C. T.; Hung, C. C.; Wu, M. S.; Phillips, A.; Yang, C. W. Epidermal growth factor and transforming growth factor-betal enhance HK-2 cell migration through a synergistic increase of matrix metalloproteinase and sustained activation of ERK signaling pathway. *Exp. Cell. Res.*, **2007**, *313*, 2367-2377.

For TOC only :